Experimental comparison of a NACA0021 airfoil in large plunging and surging motions at 90 angle of attack

Xu, Guanqun; Yu, Wei; Ferreira, Carlos; Sciacchitano, Andrea

Citation (APA)
Xu, G., Yu, W., Ferreira, C., & Sciacchitano, A. (2024). Experimental comparison of a NACA0021 airfoil in large plunging and surging motions at 90 angle of attack. *Journal of Physics: Conference Series*, *2767*(2), Article 022047. https://doi.org/10.1088/1742-6596/2767/2/022047

Important note
To cite this publication, please use the final published version (if applicable).
Please check the document version above.

PAPER • OPEN ACCESS

Experimental comparison of a NACA0021 airfoil in large plunging and surging motions at 90 ° angle of attack

To cite this article: Guanqun Xu *et al* 2024 *J. Phys.: Conf. Ser.* **2767** 022047

View the article online for updates and enhancements.

Experimental comparison of a NACA0021 airfoil in large plunging and surging motions at $90°$ angle of attack

Guanqun Xu[1], Wei Yu[1], Carlos Ferreira[1], Andrea Sciacchitano[1], Sowmya Iyer[1,2]

[1] Wind energy section, Faculty of Aerospace Engineering, Delft University of Technology, Delft, the Netherlands
[2] Department of Wind and Energy Systems, Technical University of Denmark, Lyngby, Denmark

E-mail: `G.Xu-1@tudelft.nl`

Abstract.   The topic of vortex-induced vibrations on a wind turbine blade has recently gained much attention due to its growing size and flexibility. To address this concern, a wind tunnel test was conducted to study the forced plunging and surging motion of a NACA0021 airfoil at $90°$ angle of attack. Results indicate that vortex lock-in occurred for a motion amplitude of one chord length even for a small frequency ratio (between motion frequency and static Strouhal frequency) of 0.39. Analysis of the drag coefficient, derived from the phase-averaged Particle Image Velocimetry (PIV) data, shows that a plunging airfoil experiences higher average loading than a surging airfoil, which is deemed to be more harmful considering the higher loading in the crossflow-direction due to the variation of effective angle of attack.

1. Introduction

When a wind turbine is at standstill condition, the blades are often pitched by a large angle (AoA) to cut out of the wind. In this scenario, significant vorticity may develop at both the blade's leading and trailing edges. The synchronization of the natural frequency with the structural frequency, referred to as the lock-in effect, occurs when the structural frequency gets close to the natural frequency. Consequently, vortex-induced vibration (VIV) arises, posing a substantial risk of escalating the wind turbine's fatigue load. Reviews of VIV can be found in [1], [2] and [3]. Nowadays, with the growing size of wind turbines, slender and flexible blades are more prone to fatigue due to VIV, compared to smaller-scale wind turbines.

Analyzing outcomes when aerodynamics is entwined with structural response is a complex task. To address this challenge, an initial exploration is conducted using airfoils featuring prescirbed motions. Previous numerical investigations concentrated on the wake patterns of a two-dimensional NACA0012 airfoil in a plunge motion, scrutinizing the combined effect of oscillation frequency and amplitude [4]. An experimental study has also been conducted on a pitching and surging airfoil, specifically examining the dynamic separation process at the leading edge area [5]. Studies have also been conducted on plunging and surging airfoils at low Reynolds numbers, however, the unsteady aerodynamics at larger AoAs (larger than $20°$) remain unknown [6]. The lock-in effect was examined in [7] numerically by setting a plunging airfoil

with sinusoidal motion and the lock-in effect was found. The reduced frequency is very high (near 10) while the non-denationalized plunging amplitude is relatively small (maximum 0.0005) and the AoA was set low. The lock-in effect was also studied in [8] using airfoil NACA0012. By varying the oscillating frequency and amplitude, the lock-in region was found as a "V" shape (Figure 1), as a larger motion allows for a wider oscillating frequency for the lock-in. In an airfoil wind tunnel testing in [9], a similar "V" shape was also characterized.
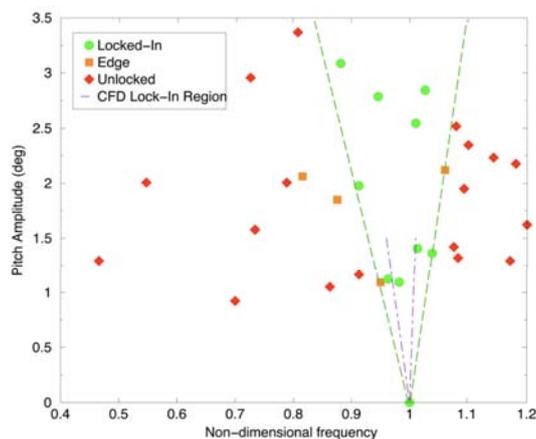
Figure 1: V-shape from [8]. Y-axis is the pitching amplitude and x-axis is the ratio between the pitching frequency and static vortex shedding frequency.

The objective of this study is to investigate the unsteady vortex shedding of a plunging and surging airfoil. In [10], a flexible wind turbine blade was simulated at AoA in the vicinity of $90°$. It was found that with a certain combination of inflow inclination angles and inflow wind speed, VIV can be triggered with the tip deflection of approximately one chord length (c). In the VIV study of [11], airfoil DU96 at AoA $90°$ was computed. In the prescribed motion computations, negative aerodynamic damping was found in the vicinity of the stationary vortex-shedding frequency. Hence, in our experiment, the AoA of the airfoil was set to $90°$ and the motion amplitude was set to $1c$ in order to emulate the AoA observed during periods of wind turbine standstill and the VIV condition.

It is important to highlight that prevailing predefined motion studies usually maintain small motion amplitudes. Nevertheless, little attention has been given to comparing unsteady aerodynamics between a plunging and surging motion. This comparison holds significance because a plunging airfoil at a $90°$ AoA resembles an edgewise excitation, while a surging airfoil resembles a flapwise excitation. Conducting a comprehensive analysis and comparison of these two motions at $90°$ AoA will facilitate a deeper comprehension of the impact of VIV on a practical, multi-degree-of-freedom wind turbine system.

2. Methodology

2.1. Wind tunnel setup

The experimental study was examined in the Open Jet Facility(OJF) at Delft University of Technology. The OJF is a closed circuit wind tunnel with an open, octagonal test section of 285×285 cm. The maximum wind speed is 35 m/s and a nominal turbulence intensity of 0.5%. The experimental setup is shown in Figure 2 with the indication of the experiment component in Table 1.

Figure 2: Experimental setup in the OJF, looking in the upstream direction. The relevant component indicated here is shown in Table 1.
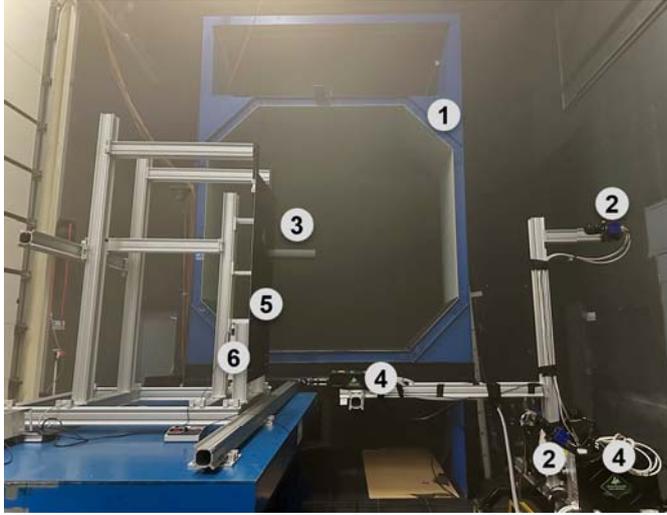
Table 1: Experimental Component

Number	Experiment component
1	Wind outlet
2	LaViSion Imager sCMOS camera
3	Airfoil model
4	Quantel Evergreen Nd:YAG laser
5	Flow protection plate
6	Plunging/surging mechanism
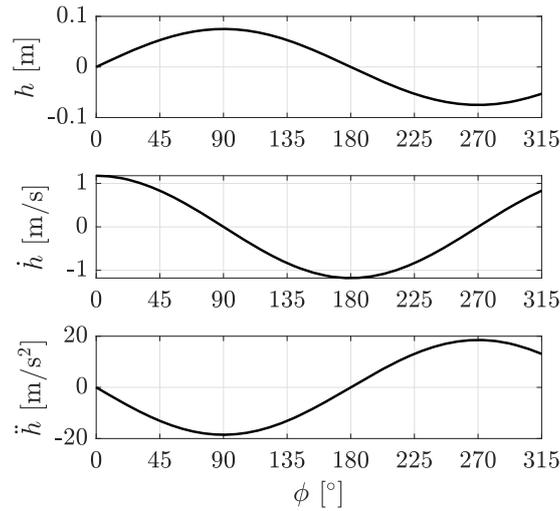
Figure 3: Designed sinusoidal motion of the airfoil: $h(\phi) = h_{amp} \sin \phi$ with $h_{amp} = 1c$. $\dot{h}$ and $\ddot{h}$ represent the velocity and acceleration of the motion separately.

2.2. Airfoil model

The NACA0021 airfoil model was used in the campaign. The model has a span of 40 cm and a chord of 7.5 cm. It is 3D printed with carbon fiber strips attached at one-quarter of the chord length on both sides of the surface. The model is designed to be rigid. The airfoil model is subjected to predefined sinusoidal motion achieved by the slider crank mechanism. The AoA is fixed at 90°. The kinematic motion of the airfoil is described as: $h(\phi) = h_{amp} \sin \phi$, where the motion amplitude h_{amp} is fixed to one chord length and ϕ is the phase of motion in each cycle. The designed motion, velocity and acceleration are shown in Figure 3. The relative position and the velocity vector are shown in Table 3 for phases at 0°, 90°, 180° and 270° for the two dynamic cases. Note that V_m' represents wind velocity due to airfoil motion V_m. V_{rel} represents the relative velocity. α_e is the effecitve AoA. Following the acquisition of the static vortex

Table 2: Experimental parameters

Parameter	Symbol	Value
Freestream velocity	U_∞	3.1 m/s
Model chord	c	0.075 m
Reynolds number (dynamic measurement)	Re	1.5×10^4
Strouhal frequency	f_{st}	6.4 Hz
Model angle of attack	AoA	90°
Model span	s	0.4 m
Model aspect ratio	AR	5.33
Motion frequnecy	f	2.5 Hz, 5 Hz
Frequency ratio	f/f_{st}	0.39 , 0.78
Motion amplitude	h_{max}	0.075 m

shedding frequency (f_{st}) through steady measurements, motion frequencies of 5 Hz and 2.5 Hz were chosen to examine the impact of motion frequency, where the frequency ratio with the static shedding frequency is 0.39 and 0.78 respectively. The amplitude of the motion remained constant at $1c$. The experimental parameters are shown in Table 2.

Table 3: Description of four phases for plunging and surging cases with wind coming from the left.

2.3. PIV measurements
Stereoscope PIV was set up to capture the flow field around the airfoil. The flow inside the tunnel was seeded with water-glycol droplets of 1 μm median diameter produced by a SAFEX

Table 4: Test matrix for dynamic measurements. Note that the root of the airfoil is $0c$ and the tip of the airfoil is $5.33c$.

No. FoV	No. phases	Spanwise position (AR/c)	No. images	Caeses	Motion frequency
3	12	5.33, 2.33	200	plunging, surging	2.5 Hz, 5 Hz
1	4	4.33, 3.33	200	plunging, surging	2.5 Hz, 5 Hz
1	4	5.83, 5.58, 5.08, 4.83	200	plunging	5 Hz

smoke generator. Quantel Evergreen Nd:YAG laser (200 mJ pulse energy, 15 Hz repetition rate, 532 nm wavelength) was used for illumination. Two LaViSion Imager sCMOS cameras (2560×2160 pixel, 16 bit, 6.5×6.5 μm pixel size) were mounted at the side of the tunnel with a certain relative angle in order to obtain the third component of the velocity. Different measurement planes in the spanwise direction were selected to compare the three-dimensional effect and the definition is shown in Figure 4. The campaign was progressed in two steps. First, the static measurement was conducted in order to find out the Strouhal vortex shedding frequency f_{st}. Then tested frequencies for dynamic measurement were chosen based on it. The test matrix for plunging cases and surging cases are shown in Table 4. And in order to obtain a larger field of view (FoV), the whole PIV system was traversed twice in the streamwise direction for tip and $2.33c$ measurement planes, for both plunging and surging cases. applying phase-averaged method, the acquisitions were acquired at 12 phases in total: 0°, 45°, 80°, 90°, 100°, 135°, 180°, 225°, 260°, 270°, 280° and 315° for the tip and $2.33c$ measurement planes. While for the other planes, phases at 0°, 90°, 180° and 270° were acquired. In this paper, the static and the dynamic measurements at $2.33c$ spanwise position are shown and the 2.5 Hz motion frequency for the dynamic cases at $2.33c$ spanwise position were selected for plunging and surging cases to compare.

2.4. Load calculation from PIV measurements

The pressure field can be extracted from the velocity field obtained from PIV measurements. As discussed in [12] and [13], the time-averaged pressure from PIV velocity statistics can be calculated from the Reynolds Averaged Navier Stokes Equation:

$$-\frac{1}{\rho}\frac{\partial(\overline{p})}{\partial x_i} = \frac{\partial(\overline{u}_i)}{\partial t} + \overline{u}_j\frac{\partial(\overline{u}_i)}{\partial x_j} - \nu\frac{\partial^2(\overline{u}_i)}{\partial x_j \partial x_j} + \frac{\partial(\overline{u_i'u_j'})}{\partial x_j} \tag{1}$$

where $\overline{u}_i$ and $\overline{u}_j$ represents the Reynolds-averaged velocity component in the i (streamwise) and j (crossflow-mwise) direction. $\overline{p}$ is the Reynolds-averaged pressure. ν is the kinematic viscosity and ρ is the air density. $\overline{u_i'u_j'}$ represents the Reynolds stress tensor. The pressure $\overline{p}$ then can be calculated using Poisson equation.

The aerodynamic force is then calculated by integrating the force in a control volume around the body [14]:

$$\bar{F}_i = -\rho\frac{\partial}{\partial t}\iint_s (x_i\overline{u}_i n_i)ds - \rho\iint_s \bar{u}_i\bar{u}_j n_j ds - \rho\iint_s \overline{u_i'u_j'}n_j ds - \iint_s \bar{p}n_i ds + \rho\nu\iint_s (\frac{\partial\bar{u}_i}{\partial\bar{x}_j}+\frac{\partial\bar{u}_j}{\partial\bar{x}_i})n_j ds \tag{2}$$

with s the outer contour of the control volume and n_i, n_j the normal unit vector (pointing outward) in the direction of i (streamwise) and j (crossflow-wise) separately. The illustration of the control volume around the airfoil is shown in Figure 5.
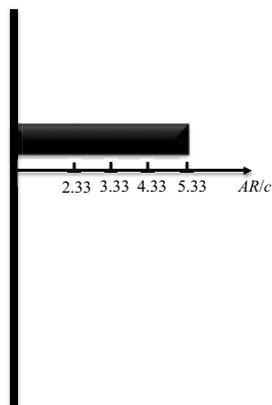
Figure 4: Spanwise position for the measurement.
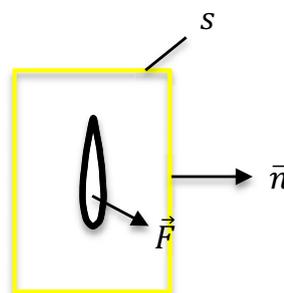
Figure 5: Control volume for calculating the aerodynamic force of the airfoil

3. Result

3.1. Static cases

(a) Streamwise velocity, $\bar{u}/U_\infty$

(b) Pressure coefficient C_P
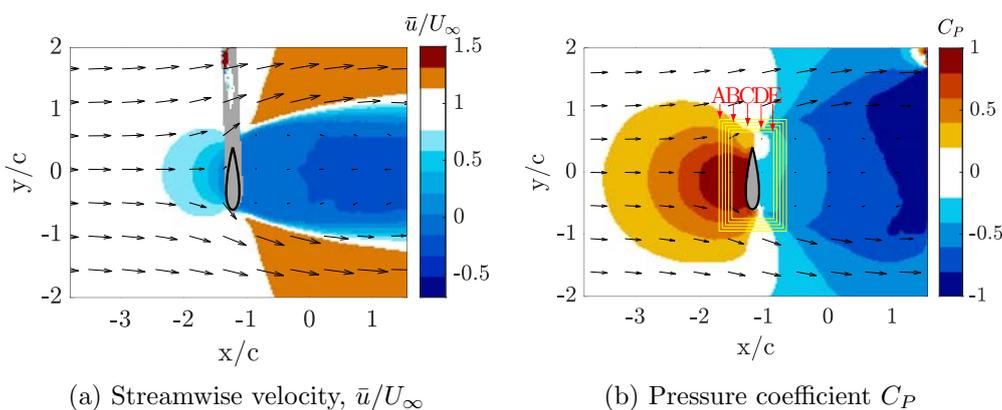
Figure 6: Static measurement at $2.33c$ spanwise position. Five control volumes from A to E are shown as yellow rectangles.

The static measurement with a larger FoV was conducted as a base comparison and Re was set to 2.5×10^4. The static case with the same Re as the dynamic measurement was conducted then with a smaller FoV only to obtain the vortex shedding frequency. The streamwise velocity $\bar{u}/U_\infty$ at $2.33c$ spanwise position is shown in Figure 6a for Re at 2.5×10^4. The PIV system traversed two times, and two FoVs in the upstream and near wake positions were stitched using the Gaussian weighting function for minimal shadow area. With the statistics from PIV flow field, the pressure coefficient C_P was calculated using Equation 1, the result is shown in Figure 6b. Note that the shadow area in the flow field was interpolated from the rest of the flow field before calculating the pressure. Then, force coefficients were obtained from control volumes of five different sizes (marked as yellow rectangles in Figure 6b) and the force coefficients are shown in Table 5.

The pressure field shown in Figure 6b indicates a pressure rise in front of the airfoil while the flow velocity decreases as the wind approaching the airfoil (shown in Figure 6a). This result matches the Bernoulli equation. In the wake region, the reverse flow was generated which

induced a lower C_p compared to the freestream pressure ($C_P = 0$). The control volumes from A to E with decreasing size have been chosen to study the sensitivity of the load calculation method. The drag and coefficients C_d show average values μ of 1.0638 , with standard deviation σ of 0.0379. Previous experiments have been conducted over airfoil NACA0021 at AoA = 90° at $Re = 1.4 \times 10^5$ [15] and at $Re = 3.5 \times 10^5$ [16]. The force coefficients at AoA = 90° for NACA0021 at $Re = 2 \times 10^5$ were extrapolated from experimental data of airfoil NACA0012, as presented in [17]. The results from literatures are listed in Table 5. μ of C_d from the experiment is the closest with the measurement in [15] while both of them diverging from the result of [16] and [17].

Table 5: Comparison of C_d with different control volume shown in Figure 6b.

	A	B	C	D	E	μ	σ	[15]	[16]	[17]
C_d	1.0919	1.0638	1.0326	1.0124	1.1013	1.0604	0.0379	0.87	1.6635	1.8

There are certain errors and uncertainties from this campaign that lead to the divergence of force coefficients. Firstly, it comes from the interpolated data near the airfoil surface for the pressure calculation. The accuracy of interpolation influenced the accuracy of the pressure field, the error was then integrated in the control volume which led to a higher error. Secondly, as one end of the airfoil in the campaign was set free, spanwise flow existed in the system. While the result was shown in two dimensional, the third component in the flow will influence the pressure field calculation and thus the load coefficient. Thirdly, the PIV system has its uncertainty in cross-correlation, and in peak locking, spatial resolution, etc [18], which may lead to different results compared to either the pressure tap measurement ([15] and [16]) or the extrapolation ([17]). On the other hand, as the test conditions from case to case are different (e.g., the blockage correction was not mentioned in [16]), it is hard to draw a conclusion for the divergence. Lastly, the extrapolation result presented in [17] has been proved inaccurate [19].

3.2. Dynamic cases

The vorticity ($\bar{\omega}c/U_\infty$) of the plunging and surging cases at 2.5 Hz with $1c$ motion amplitude are shown in Figure 7 for the the left column and the right column separately. Phase angle $\phi = 0°$, 90°, 135°, 180°, 225° and 270° are listed in the order of vortex generation for comparison. For the plunging airfoil, there exists a long shear layer (approximately $4c$ in length) shedding from the leading edge and trailing edge of the airfoil. For the surging case, the shear layer length varied from phase to phase, depending on the perceived wind. It is also obvious that, for a plunging case, the wake is tilted according to the change of effective AoA. For the surging case, the motion velocity is smaller than the free stream velocity and they are parallel. Consequently, the effective AoA is always 90°, which explains that the wake is at the downwind position and is parallel to the wind across all phases.

For the plunging airfoil, vortex shedding initiates from $\phi = 90°$ when the airfoil reaches the upmost position in a cycle. As the airfoil changes direction and moves downwards from $\phi = 90°$ to $\phi = 135°$, it reaches peak acceleration, accompanied by a clot of vortices with negative strength separated from the main shear layer in the streamwise direction from $x/c = 1.4$ to $x/c = 2.6$. As the airfoil goes further downwards, from $\phi = 180°$ to $\phi = 225°$, vortices with positive strength start to shed from the wake. During these two phases, motion velocity starts to slow down, and the inertia from the flow makes the vortex travel faster, and in the end separate from the body. A different starting point at $\phi = 180°$ is shown for surging cases as at $\phi = 180°$, the perceived velocity is the lowest as the motion velocity is the lowest shown in

(a) Plunging cases   (b) Surging cases
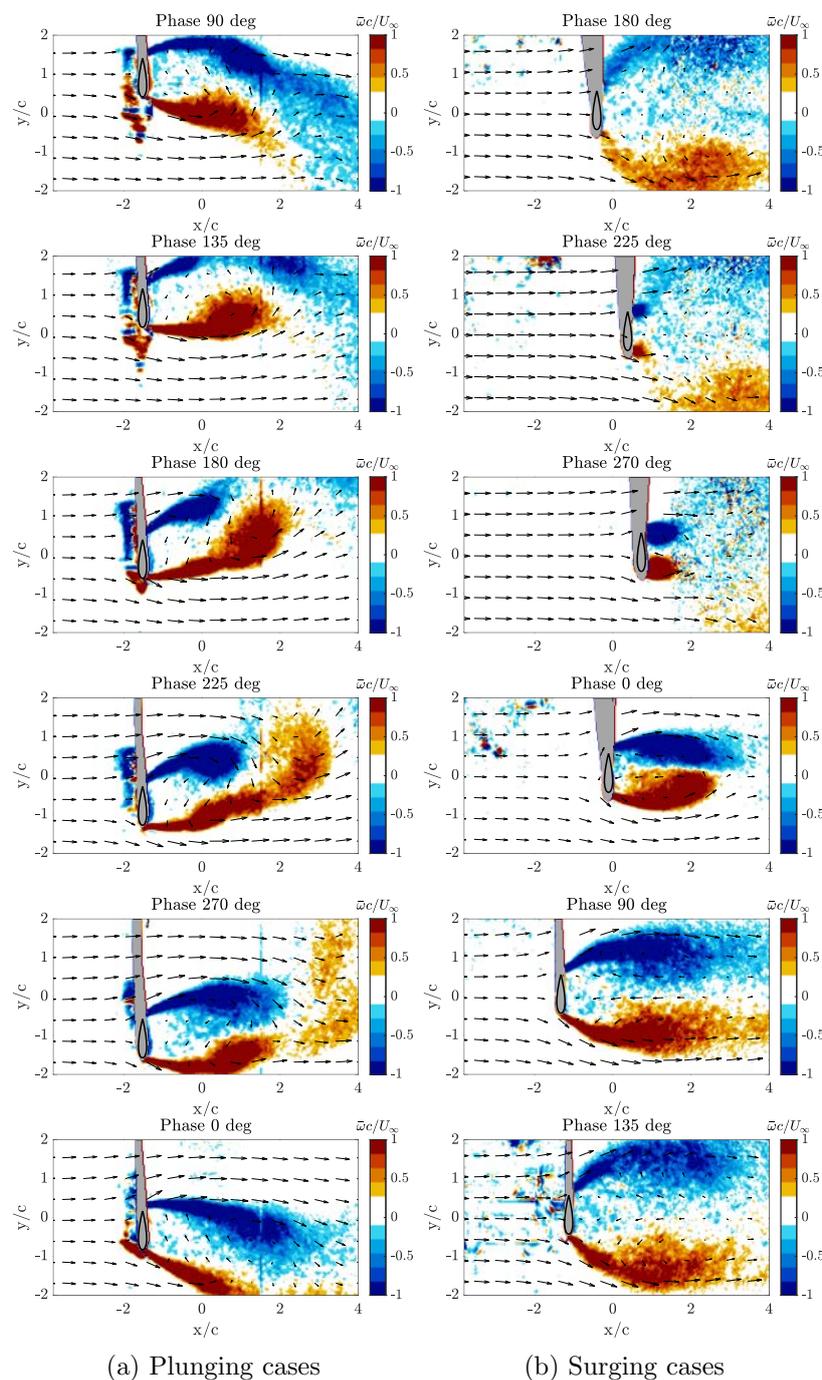
Figure 7: Vorticity ($\bar{\omega}c/U_\infty$) around the surging airfoil (the left column) and the plunging airfoil (the right column) at 2.5 Hz, at $2.33c$ spanwise location.

Figure 3. As the airfoil keeps surging to $\phi = 135°$, the size of vortices keeps expanding and up until $\phi = 180°$, a new pair of vortices starts to generate. Both the results from plunging and surging cases show that during one motion cycle, a solitary pair of vortices is observed to shed from the airfoil's wake. So, instead of staying at the static vortex shedding frequency, the vortex shedding frequency was synchronized with the motion frequency. Based on the definition of lock-in, this result serves as a clear manifestation of the lock-in effect. When forced frequency f is at

2.5 Hz, the frequency ratio $f/f_{st} = 0.39$, which is far away from the static Strouhal frequency f_{st}. However, a typical lock-in region has a wider frequency band for high motion amplitude, lock-in can still happen due to the large motion of $1c$. As discussed in [20], the lock-in region is amplitude-dependent and when the amplitude reaches the lowest limit to trigger lock-in, it would only happen when $f/f_{st} = 1$.
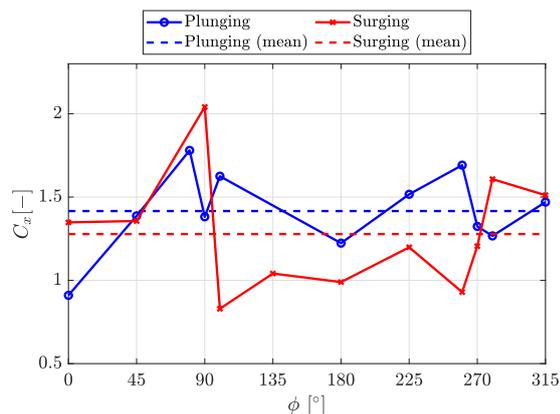
Figure 8: Streamwise force coefficient C_x in a cycle for 2.5 Hz in $2.33c$ spanwise position.
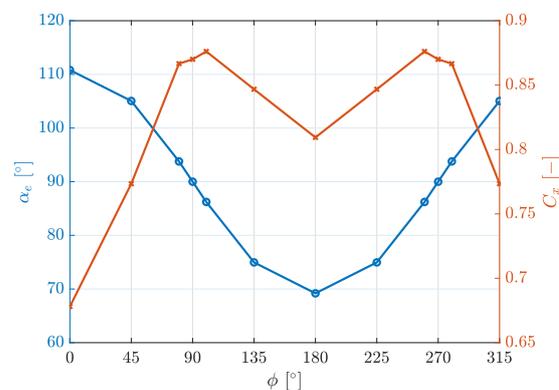
Figure 9: Effective AoAs (left axis), α_e, for the measured phases for the plunging airfoil and estimated streamwise force coefficient C_x interpolated from polar in [15] based on α_e.

The streamwise force coefficient C_x in a cycle was calculated from the phase-averaged velocity field and is shown in Figure 8. C_x of the plunging case in the experiment is shown as the blue solid line with circles. The estimated C_x of plunging cases is shown as the red line with crosses in Figure 9. These estimated values were obtained by interpolating the polar from [15], based on the effective AoA α_e of the airfoil. α_e is shown as the blue line with circles in Figure 9. Comparing the result from the experiment and the estimated values, the overall trend follows the same: two peak regions are shown near $\phi = 90°$ and $270°$. In these two regions, α_e is near $90°$ which brings the highest projection of load in the streamwise direction. On the other hand, these two regions have the highest acceleration, as shown in Figure 3. According to a low-order model of a surging wing proposed in [21], the force acting on the wing can be dissected into two components: the non-circulatory part and the circulatory part. The non-circulatory part is attributed to the inertial effects of the added mass. Consequently, when ϕ approaches $90°$ and $270°$, the drag coefficient from the added mass term reaches its peak, making the most substantial contribution to the non-circulatory part in C_x. It is important to note that the estimated result is based purely on α_e. For the plunging case, the unsteady force from the motion and the vortex shedding can have a complicated effect on the force the airfoil perceived. Under this consideration, the quasi-static estimation cannot represent the detailed value.

The experiment result of a surging airfoil is shown as the red solid line with crosses in Figure 8. If C_x is estimated with α_e, then within a cycle C_x is a fixed value. However, the value dropped from $\phi = 90°$ and increased back from $\phi = 270°$. During this surging period from $\phi = 90°$ to $270°$, the airfoil is moving along with the direction of the wind, thus the perceived wind is lower than the incoming wind, which leads to the decrease of force and thus C_x, compared to the phases when the airfoil is moving against the wind. In the surging case, the airfoil is moving while pushing the air around it, and the non-circulatory force is influenced based on the acceleration and the mass of air being moved. Meanwhile, the circulatory part of the force is nonlinearly influenced by the motion speed, the circulation of the flow, etc [21], which needs to be further analyzed in the future.

The results of the two dynamic scenarios distinctly demonstrate the fluctuating forces experienced by the airfoil throughout a cycle. In the case of plunging, the average C_x over a cycle is 1.42, exceeding the corresponding surging case value of 1.28. Apart from the higher force in the streamwise direction for plunging, there is also a crossflow-wise component due to the variation of α_e. Therefore, under the same dynamic motion condition of frequency and amplitude, plunging cases can be considered more "harmful" as higher forces are expected in both the streamwise and crossflow-wise direction. Considering a freely vibrating airfoil, plunging motion can add more fatigue load in the long term.

4. Conclusion

This work presents an experiment on a plunging and surging NACA0021 airfoil at $90°$ angle of attack to study the effect of lock-in. Different from previous studies, a large motion amplitude of one chord was set, and the result shows that even though the motion frequency is far from the static vortex shedding frequency, the motion amplitude is large enough to trigger the lock-in, as shown directly from the flow field result.

Specifically, the streamwise force coefficient C_x was obtained from the PIV statistics using the Reynolds-average Navier-Stokes equation and control volume method. C_x in a cycle for the plunging case shows a larger mean value than the surging case. Considering the force component in the crossflow-wise direction, it is considered to be more harmful compared to surging cases. The result of this campaign indicates the direction of the VIV study on the wind turbine blade, while further study needs to be done to verify the relation to the real wind turbine blade cases.

References

[1] Bearman P W 1984 *Annual review of fluid mechanics* **16** 195–222
[2] Williamson C H and Roshko A 1988 *Journal of fluids and structures* **2** 355–381
[3] Sarpkaya T 2004 *Journal of fluids and structures* **19** 389–447
[4] Young J and Lai J C 2004 *AIAA journal* **42** 2042–2052
[5] Dunne R and McKeon B J 2015 *Experiments in Fluids* **56** 157
[6] Choi J, Colonius T and Williams D R 2015 *Journal of Fluid Mechanics* **763** 237–253
[7] Young J and Lai J C 2007 *AIAA journal* **45** 485–490
[8] Besem F M, Kamrass J D, Thomas J P, Tang D and Kielb R E 2016 *Journal of Fluids Engineering* **138** 011204
[9] Tang D and Dowell E H 2014 *AIAA journal* **52** 1170–1179
[10] Heinz J C, Sørensen N N, Zahle F and Skrzypiński W 2016 *Wind Energy* **19** 2041–2051
[11] Skrzypiński W, Gaunaa M, Sørensen N, Zahle F and Heinz J 2014 *Wind Energy* **17** 1495–1514
[12] Van Oudheusden B W, Scarano F, Roosenboom E W, Casimiri E W and Souverein L J 2007 *Experiments in fluids* **43** 153–162
[13] Van Oudheusden B, Casimiri E and Scarano F 2008 *The Aeronautical Journal* **112** 197–205
[14] Rival D E and Oudheusden B v 2017 *Experiments in Fluids* **58** 20
[15] Holst D, Balduzzi F, Bianchini A, Church B, Wegner F, Pechlivanoglou G, Ferrari L, Ferrara G, Nayeri C N and Paschereit C O 2019 *Journal of Engineering for Gas Turbines and Power* **141** 051015
[16] Swalwell K E, Sheridan J, Melbourne W *et al.* 2001 The effect of turbulence intensity on stall of the naca 0021 aerofoil *14th Australasian fluid mechanics conference* pp 941–944
[17] Sheldahl R E and Klimas P C 1981 Aerodynamic characteristics of seven symmetrical airfoil sections through 180-degree angle of attack for use in aerodynamic analysis of vertical axis wind turbines Tech. rep. Sandia National Labs., Albuquerque, NM (USA)
[18] Ragni D, Van Oudheusden B and Scarano F 2011 *Experiments in Fluids* **51** 361–371
[19] Melani P F, Balduzzi F, Ferrara G and Bianchini A 2019 An annotated database of low reynolds aerodynamic coefficients for the naca0018 airfoil *AIP Conference Proceedings* vol 2191 (AIP Publishing)
[20] Karniadakis G E and Triantafyllou G S 1989 *Journal of Fluid Mechanics* **199** 441–469
[21] Babinsky H, Stevens R J, Jones A R, Bernal L P and Ol M V 2016 Low order modelling of lift forces for unsteady pitching and surging wings *54th AIAA aerospace sciences meeting* p 0290